ELSEVIER

An input function estimation method for FDG-PET human brain studies ☆

Hongbin Guo[a],*, Rosemary A. Renaut[a], Kewei Chen[b,c]

[a]Department of Mathematics and Statistics, Arizona State University, Tempe, AZ 85287-1804, USA
[b]Banner Alzheimer's Institute, Phoenix, AZ 85006, USA
[c]Banner Good Samaritan Positron Emission Tomography Center, Phoenix, AZ 85006, USA

Abstract

Background: A new model of an input function for human [^{18}F]-2-Deoxy-2-fluoro-D-glucose fluoro (FDG) positron emission tomography (PET) brain studies with bolus injection is presented.
Methods: Input data for early time, roughly up to 0.6 min, were obtained noninvasively from the time–activity curve (TAC) measured from a carotid artery region of interest. Representative tissue TACs were obtained by clustering the output curves to a limited number of dominant clusters. Three venous plasma samples at a later time were used to fit the functional form of the input function in conjunction with obtaining kinetic rate parameters of the dominant clusters, K_1, k_2 and k_3, using the compartmental model for FDG-PET. Experiments to test the approach used data from 18 healthy subjects.
Results: The model provides an effective means to recover the input function in FDG-PET studies. Weighted nonlinear least squares parameter estimation using the recovered input function, as contrasted with use of plasma samples, yielded highly correlated values of $K = K_1 k_3/(k_2 + k_3)$ for simulated data, a correlation coefficient of 0.99780, a slope of 1.019 and an intercept of almost zero. The estimates of K for real data by graphical Patlak analysis using the recovered input function were almost identical to those obtained using arterial plasma samples, with correlation coefficients greater than 0.9976, regression slopes between 0.958 and 1.091 and intercepts that are virtually zero.
Conclusions: A reliable semiautomated alternative for input function estimation that uses image-derived data augmented with three plasma samples is presented and evaluated for FDG-PET human brain studies.
© 2007 Elsevier Inc. All rights reserved.

Keywords: Input function estimation; FDG-PET; Quantification

1. Introduction

Positron emission tomography (PET) is a widely used neuroimaging technique that, among others, assists with disease diagnosis, treatment evaluation and study of brain function. In addition to their visual and qualitative assessments, PET images can provide quantitative estimates of physiological or metabolic parameters of interest. We are interested in dynamic [^{18}F]-2-Deoxy-2-fluoro-D-glucose fluoro (FDG) PET, which permits the estimation of the

cerebral metabolic rate for glucose (CMRglc) and has been used for analyses of brain diseases associated with aging. The focus of this study was on the estimation of the input function, the time-varying radiotracer concentration in plasma, which is required in quantifying data from dynamic FDG-PET images [1].

While the invasive gold standard of arterial plasma sampling procedure to obtain the input function has long been suggested, its invasive nature has limited its routine use in basic research, especially in clinical PET studies. Many alternative methods for FDG-PET and other tracers have been proposed. These include obtaining arterialized venous plasma samples [2], using population-based input functions [3–5], estimating the rate constants using a multichannel blind identification without input function [6] and simultaneously estimating (SIME) the input and the kinetic parameters for a limited number of brain regions

[7,8]. Other methodologies include constructing an image-derived input function, possibly combined with limited plasma sampling and/or the SIME approach [9–12]. Noting the risks and discomfort associated with any kind of plasma sampling, the PET Neuroimaging Working Group [1] recommended that, where possible, PET studies be accomplished through the use of a completely image-derived input function. We make further progress toward this end by proposing a new functional model for the input function of FDG-PET that is then used to extend an existing image-derived approach [9].

A new functional form of the input function for dynamic FDG-PET brain studies using bolus injection is presented in Section 2. In Section 3, we describe a nested optimization method to simultaneously estimate the input model parameters and the kinetic rate parameters, K_1, k_2 and k_3, from a limited number of dominant tissue types. Results and validation of the proposed method for the clinical study and for simulated data are given in Section 4. Additional comments about the method are discussed in Section 5, and conclusions are provided in Section 6.

2. A model for the input function

2.1. Rationale

We distinguish between the characteristics of the input function over roughly the first half minute and those at a later time. In the very early time after the tracer is rapidly administered, the input function as seen in the plasma, denoted by $u_p(t)$, increases rapidly to a peak value and then quickly drops (see crosses in Fig. 1).
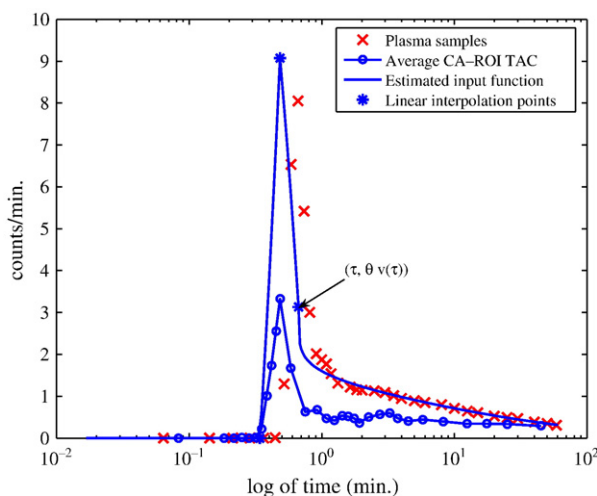

Fig. 1. Comparison of the arterial plasma samples (crosses), average CA-ROI region TAC (solid line with open circles) and estimated input function (solid line with three discrete asterisks). Also illustrated with the three asterisks are the time at which the average tracer activity was initiated in the CA-ROI τ_0, the time point for the peak value τ_p, the point of continuity τ between windows W_1 and W_2 and the three plasma samples used for the fit. Time is expressed on a logarithm scale, hence emphasizing the effects for early time.

These sharp increase and decrease can be approximated by two line segments, one upward from left of the peak to the peak and the other downward from the peak. Three nodes, $(\tau_0, 0)$, (τ_p, v_p) and (τ, v_τ), that define the line segments (see Section 2.2.1) are generated using image-derived data from carotid artery regions of interest (CA-ROIs). Here, $v(t)$ denotes the average image-derived whole blood TAC of the CA-ROIs, and the linear segments are scaled to account for partial volume effects and red cell fraction (hematocrit).

After the early interval of roughly 0.5 min, image-derived data are subjected to greater contamination of tracer spillover from tissue to blood. We therefore modeled the input data after the initial interval without using image-derived data but using a limited number of intravenous plasma samples. The piecewise-continuous and parameter-dependent formulation for the estimated input function u_e is given by

$$u_e(t, \theta, \lambda, \delta) = \begin{cases} 0 & t \in [0, \tau_0] \\ \theta v_p \frac{t - \tau_0}{\tau_p - \tau_0} & t \in [\tau_0, \tau_p] \\ \theta \frac{v_\tau(t - \tau_p) + v_p(\tau - t)}{\tau - \tau_p} & t \in [\tau_p, \tau] \\ \theta v_\tau e^{-\lambda(t - \tau)^\delta} & t > \tau. \end{cases} \quad (1)$$

where the interval $[0, \tau]$ defines the early time window W_1, typically $\tau < 0.6$ min, and $W_2 = [\tau, T]$ is the second window, $T \approx 60$ min. The parameter θ is introduced to account for partial volume effects and hematocrit in the measurement of the tracer concentration in $v(t)$.

2.2. Image-derived input function data

The curve associated with the image data from CA-ROIs is obtained from the PET frames using the same protocol and code as those used in Reference [9]. The initial time frames up to time 2 min are summed so as to emphasize those voxels that show the tracer in the CA-ROIs, typically three to five slices in the lower portion of the brain [for FDG-PET data acquired with the 951/31 emission computerized axial tomography (ECAT) scanner] and from which whole blood TACs for each observed CA-ROI can be calculated. Averaging over these curves yields the data that define the average whole blood TAC $v(t)$ (see the solid line with open circles in Fig. 1). We can see that $v(t)$ provides crucial subject- and situation-dependent information on the input function by providing the times at which the tracer reaches the CA-ROI, τ_0, and then the time at which it peaks in the blood, τ_p. The delay between u_p and $v(t)$ is merely indicative of the shift due to their measurement from different sources. An immediate visual comparison shows the underestimation of $v(t)$ as compared with $u_p(t)$ due to partial volume effects and hematocrit, which is accounted for in Eq. (1) through the scaling of $v(t)$ inversely proportionally to its recovery from the image by parameter θ.

2.2.1. Piecewise linear approximation to the image-derived data for an early time

Given the image-derived data for $v(t)$, a piecewise linear approximation for $v(t)$ is defined in Model (1), which depends on the automatic selection of the three time points (τ_0, τ_p and τ). It is easy to determine τ_p as the point in the sampled data at which the highest intensity value $v_p = v(\tau_p)$ is achieved. The point τ_0 provides an estimate of the initiation time of activity, prior to which there is effectively no signal [14]. To facilitate the automatic estimation of τ_0, we selected it as the point after which $v(t)$ remains greater than $0.02v_p$.

The significance of the time point τ, which is a time point shortly after τ_p, is to ensure that the input on W_1 can be well approximated by two line segments; on W_2, it can be well modeled by $u_{W_2} = \theta v_\tau e^{-\lambda(t-\tau)^\delta}$ (see further details comparing this analytical form with other analytical expressions in Reference [15]). While it can be determined automatically, it cannot be simply predetermined to be a fixed number of points after the peak because noise may contaminate a chosen point. We therefore chose a relatively simple automatic way to select τ. Two straight line least squares fits were used. We formed one linear data fit through the point τ_p as well as the next two points to the right of τ_p and a second linear data fit through the last of these and two more to the right. Their point of intersection defines both τ and the value v_τ, which is most likely not one of the discrete values of $v(t)$.

3. Methods

A nested optimization method for recovering the input function $u_e(t)$ and the kinetic rate parameters of representative tissue TACs (TTACs) obtained from clustering is presented. The recovered u_e can then be used to calculate kinetic parameters and

$$K = \frac{K_1 k_3}{k_2 + k_3} \qquad (2)$$

for additional TTACs.

3.1. Clustering the PET data

The fast clustering method described in detail in Reference [13] was used to find p representative TTACs, $y_{TAC}^{(i)}(t)$, $i = 1 \cdots p$, for the whole brain excluding nonbrain, blood vessel and cerebrospinal fluid regions. Throughout this article we use (i) in superscript to label cluster i and assume that the cluster labeling is ordered such that the first cluster is the largest. The advantage of clustering is that it provides an automated way in which to segment the data into tissue groups of similar functional activity.

3.2. An algorithm for recovering the input function

In the compartmental model [16] for FDG-PET, the ideal TTAC $y(t)$ at a given voxel or for a specific brain tissue ROI is given analytically by convolution ($\otimes$) of the instantaneous response function (IRF) with input $u(t)$

$$y(t) = u(t) \otimes \left(\frac{K_1 k_3}{k_2 + k_3} + \frac{K_1 k_2}{k_2 + k_3} e^{-(k_2+k_3)t} \right). \qquad (3)$$

The IRF is the term within the parentheses and depends on the specific tissue response to the tracer. K_1 is the transport rate from plasma to brain tissue with units ml/100g/minute, k_2 is the transport rate back from the brain to the blood vessel expressed as min^{-1} and k_3 is the phosphorylation rate of intracellular FDG by hexokinase enzymes to FDG-6-phosphate also expressed as min^{-1}. Because the scanning interval of 60 min is relatively small, it will be difficult to accurately estimate the dephosphorylation rate of intracellular FDG-6-phosphate back to FDG, k_4 [17]. We thus set k_4, which is itself small, to zero.

Typically, kinetic parameters for cluster curve $y^{(i)}$, given by Eq. (3), can be obtained by the minimization of $\Phi^{(i)}$,

$$\Phi^{(i)}\left(x^{(i)}, \alpha^{(i)}\right) = \sum_{j=1}^{n} w_j \left(y_{TAC}^{(i)}(t_j) - \alpha^{(i)} \cdot y^{(i)}(t_j) \right.$$
$$\left. - \left(1 - \alpha^{(i)}\right) \cdot u(t_j) \right)^2. \qquad (4)$$

$\alpha^{(i)}$ accounts for both partial volume and spillover effects for cluster i, and the rate constants are components of $\mathbf{x}^{(i)} = [K_1^{(i)}, k_2^{(i)}, k_3^{(i)}]$. The contributions from each time point are weighted by w_j. Ideally, these are the inverse values of the variances of the data of each frame and are different for different TTACs. Because of the difficulty of estimating the variances, they are set to the time durations of the relevant time frames as practiced in the study reported in Reference [18]. To define a feasible space for the parameters, we imposed bound constraints.

It is usually assumed that the values for $u(t_j)$ used in Eq. (4) are measured values of the input function. In contrast, we intended to use the functional form shown in Eq. (1). With respect to the dominant first cluster, the parameters θ, λ, δ of the input function $u_e(t)$ can be recovered simultaneously with the kinetic rate constants. This is accomplished in a two-stage process. Specifically, notice that for any given value of θ, parameters λ, δ can be obtained as the solutions of

$$[\lambda(\theta), \delta(\theta)] = \text{argmin}_{\lambda, \delta} \sum_{l=1}^{3} \left[\theta v(\tau) e^{-\lambda(\tilde{t}_l - \tau)^\delta} - u_p(\tilde{t}_l) \right]^2, \qquad (5)$$

using three intravenous plasma samples, $(\tilde{t}_l, u_p(\tilde{t}_l))$, $l = 1, 2, 3$. Therefore, at each iteration in the minimization of $\Phi^{(1)}(\mathbf{x}^{(1)}, \alpha^{(1)}, \theta)$, noting now the introduced dependence on the recovery coefficient θ, Eq. (5) can be solved to obtain updates of λ and δ.

Input:
1. Bounds for $K_1^{(i)}, k_2^{(i)}, k_3^{(i)}, \theta, \alpha^{(i)}$ as defined in (8).
2. Plasma samples, $u_{bs}(\tilde{t}_l), l = 1, 2, 3$.
3. Data defining linear approximation to the CA-ROI TAC
   for initial time interval: time points $[\tau_0, \tau_p, \tau]$, and values $[0, v_{\tau_p}, v_\tau]$.
4. Cluster TTACs, $y_{TAC}^{(i)}(t_j), i = 1, 2, \ldots, p$.
5. Scanning durations, $w_j = \Delta t_j, j = 1, 2, \ldots, n$.
6. Time points for each frame, $t_j, j = 1, 2, \ldots, n$.

Initialization:
$K_1^{(i)} = 0.08, k_2^{(i)} = 0.2, k_3^{(i)} = 0.04, \alpha^{(i)} = 0.95, \theta = 2$ and $\lambda = -1, \delta = 0.3$.

Evaluate objective function Φ by (6)

Approximate gradient and Hessian of Φ respect to variables $K_1^{(i)}, k_2^{(i)}, k_3^{(i)}, \theta, \alpha^{(i)}$.

$\alpha^{(i)}$

Update $y^{(i)}(t_j)$ by (3)

$K_1^{(i)}, k_2^{(i)}, k_3^{(i)}$

Calculate new line search direction of current *fmincon()* iteration step.

Update $u_e(t_j, \theta, \lambda, \delta)$ by (1)

Update solution $K_1^{(i)}, k_2^{(i)}, k_3^{(i)}, \theta, \alpha^{(i)}$.

Update $\lambda(\theta), \delta(\theta)$ for new θ by (5) using plasma samples and $v(\tau)$ with constraints $-100 \le \lambda \le 0, 0 \le \delta \le 2$.

N

θ

Test convergence

Y

Output:
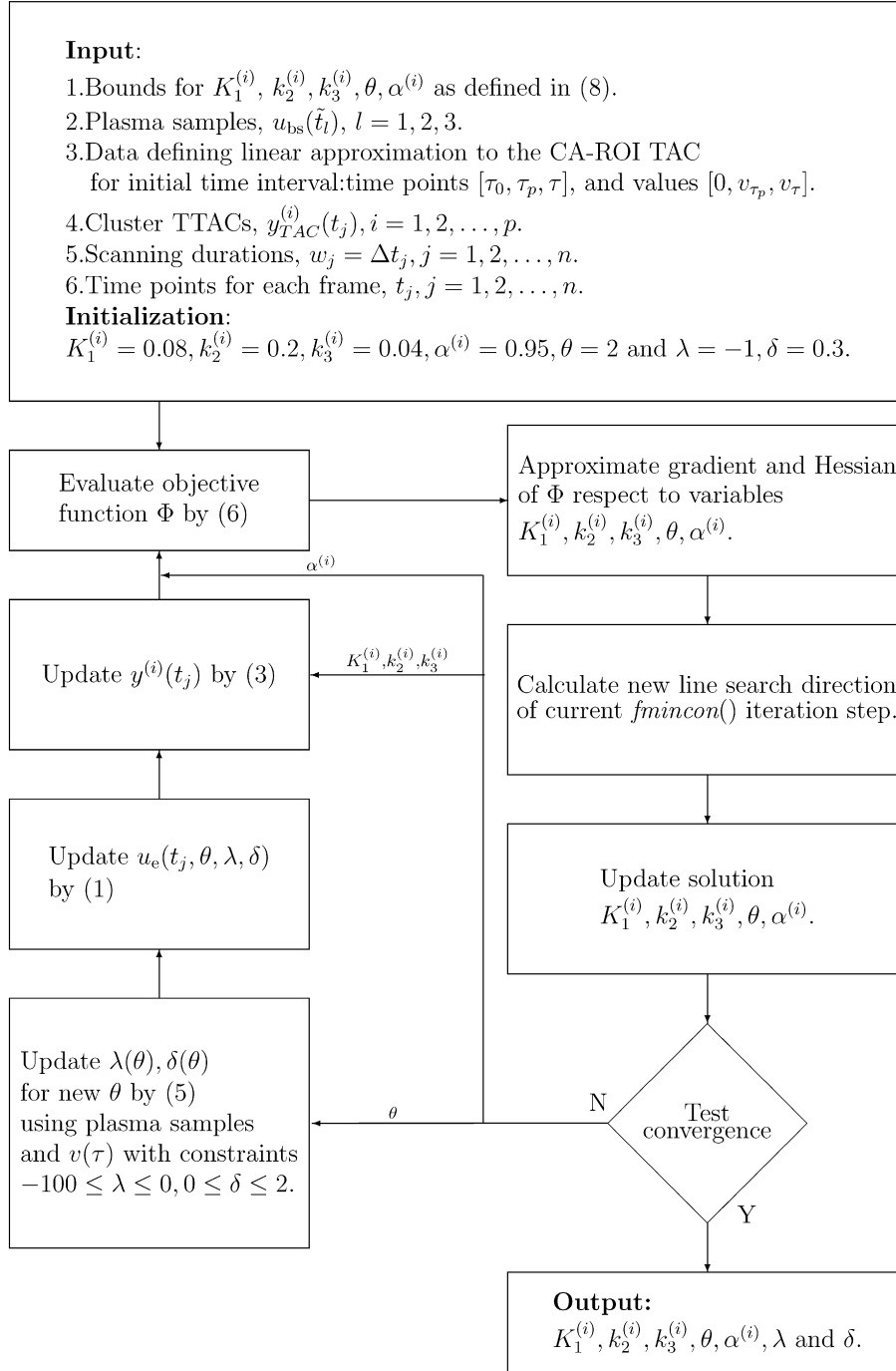$K_1^{(i)}, k_2^{(i)}, k_3^{(i)}, \theta, \alpha^{(i)}, \lambda$ and δ.

Fig. 2. Flowchart detailing the steps of the nested optimization.

To make the estimation of the input function more robust, we note that the input function is common to all TTACs and thus propose that the optimization be performed simultaneously over p clusters with the cost function

$$\Phi(\mathbf{x}, \alpha, \theta) = \sum_{i=1}^{p} \Phi^{(i)}\left(\mathbf{x}^{(i)}, \alpha^{(i)}, \theta\right) \qquad (6)$$

where $\mathbf{x} = (\mathbf{x}^{(1)}, \ldots, \mathbf{x}^{(p)})$ and $\alpha = (\alpha^{(1)}, \ldots, \alpha^{(p)})$.

In summary, the nested optimization method, illustrated in the flowchart provided in Fig. 2, is formulated as follows:

$$\min_{\mathbf{x}, \alpha, \theta} \Phi(\mathbf{x}, \alpha, \theta) \qquad (7)$$

subject to constraints

$$1.2 \le \theta \le 4,\ 0.9 \le \alpha^{(i)} \le 1,\ 0.015 \le K_1^{(i)} \le 0.3,$$
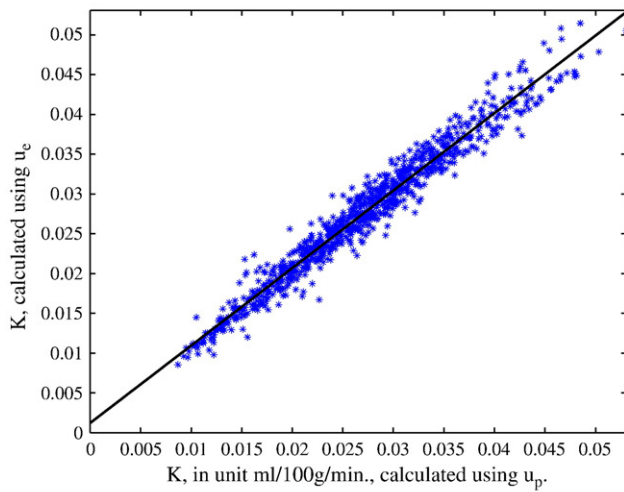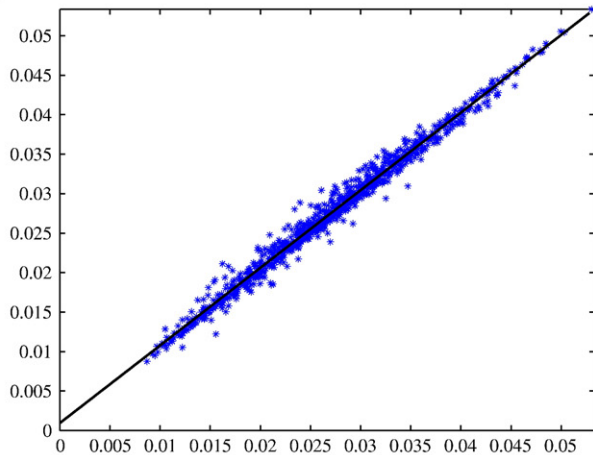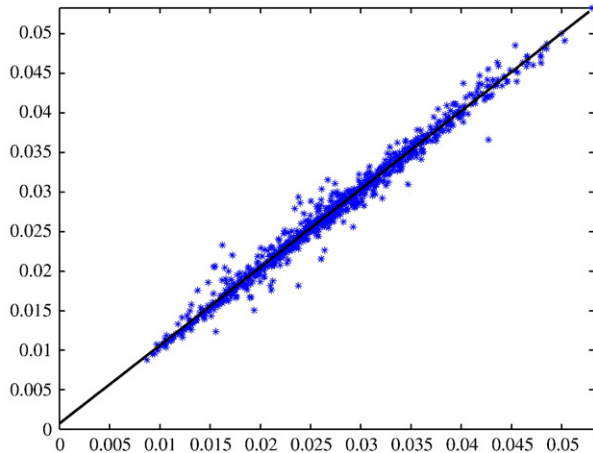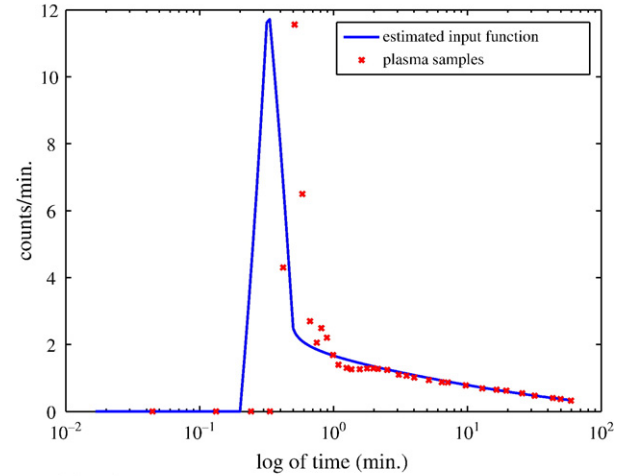$$0.024 \le k_2^{(i)} \le 0.54,\ 0.01 \le k_3^{(i)} \le 0.2. \qquad (8)$$

A p = 1 correlation .97968

B p = 2 correlation .99269

C p = 3 correlation .99115

Fig. 3. Linear regression for parameter K, calculated using Eq. (2), with u_p as compared with u_e obtained using 1, 2 and 3 clusters. Regression was carried out over 50 clusters for all 18 subjects.

A Without alignment
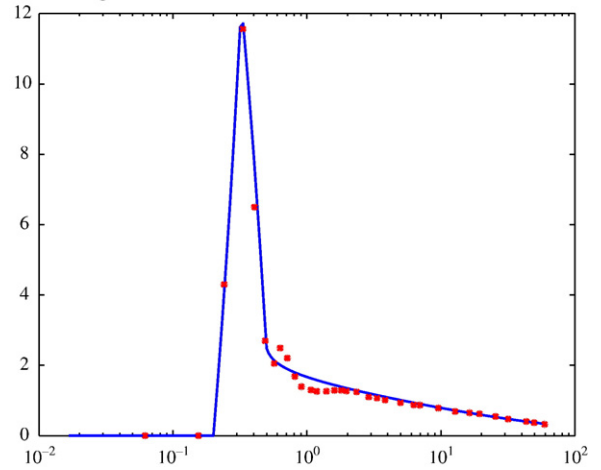

B With alignment

Fig. 4. The recovered input function $u_e(t)$ as compared with arterial plasma samples, $u_p(t)$. Illustrated are the data given on a logarithm time scale (A) and the same data with $u_e(t)$ shifted to account for the time delay relative to $u_p(t)$ (B).

The Matlab 7.0 function *fmincon* from the Optimization Toolbox version 3.0.2 [19] is used for carrying out this constrained minimization. The bounds used are based on experimental results [17] for both gray and white matter from 13 subjects, but with doubling of upper bounds and halving of lower bounds such that the feasible space is not too conservatively estimated. The time delay between the TTACs and the input function is removed by automatically shifting the TTACs such that the first peak of each is aligned with v_{τ_p}.

4. Results

Experiments that assess the method with respect to the number of clusters, visually examine the recovered input function as compared with plasma-sampled data, demonstrate the robustness of the parameters defining the input function, use the recovered input function in graphical Patlak analysis as compared with using the plasma-sampled

data and compare the calculation of Eq. (2) using the kinetic parameters obtained by nonlinear least squares for both plasma-sampled input data and the recovered input function are reported.

4.1. Clinical data set

The retrospective PET data available were collected using a 951/31 ECAT scanner (Siemens, Knoxville, TN, USA) with an identical scanning protocol for each subject. An initial 20-min transmission scan was acquired for attenuation correction, and an intravenous bolus of 10 mCi of FDG was administered over 5–10 s under resting condition. PET images were reconstructed using a filtered back-projection algorithm with a Hanning filter of 0.40 cycles per voxel. There were 31 transaxial slices of 128×128 voxels, each voxel of size 0.18776×0.18776 cm^2, with a center-to-center slice separation of 3.375 mm and a 10.8-cm axial field of view. The final reconstructed PET images have an in-plane resolution of 9.5-mm full-width at half-maximum (FWHM) in the center of the field of view and an axial resolution of 5.0- to 7.1-mm FWHM.

Scanning durations, given in minutes, for the reconstructed frames were 0.2, 8×0.0333, 2×0.1667, 0.2, 0.5, 2×1, 2×1.5, 3.5, 2×5, 10 and 30. (The noisy first frame was excluded from the analyses.) Total session duration was 60 min. The arterial plasma samples were drawn every 5 s for the first minute, every 10 s for the second minute, every 30 s for the next 2 min and then at 5, 6, 8, 10, 12, 15, 20, 25, 30, 40, 50 and 60 min, yielding a discrete representation of the plasma-sampled function expressed as counts per milliliter per minute, denoted by $u_p(t_j)$ for $j = 1, \ldots, 34$.

4.2. Dependence on the number of clusters

Using a greater number of cluster TTACs in minimizing the cost function in Eq. (7) increases the computational complexity. The nested optimization of the constrained cost function is solved using $p = 1$, 2 and 3 clusters (out of a total of 5 clusters) to assess the dependence on p of the recovered input and resulting estimated K by Eq. (2). The recovered input u_e for each choice of p, namely u_e with the converged values for θ, λ and δ, is then used in standard nonlinear
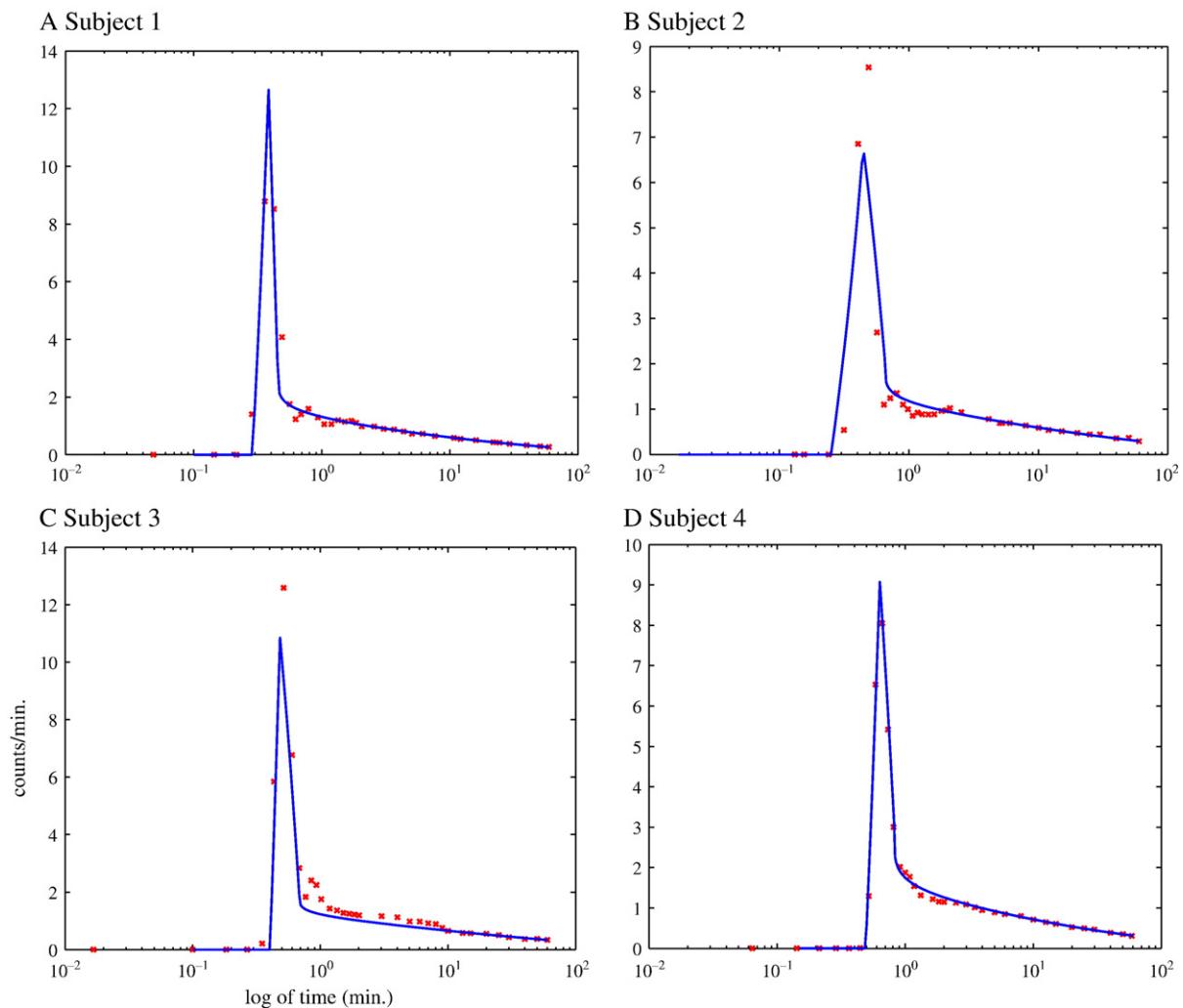

Fig. 5. Comparison of shifted estimated input u_e, continuous line and u_p for Subjects 1–4 in Panels (A)–(D), respectively.

Table 1
Constants $\alpha^{(i)}$ Eq. (7). of each cluster and parameters defining u_{W_2} obtained in the proposed method

Subject	θ	λ	δ	$\alpha^{(1)}$	$\alpha^{(2)}$
1	2.049	0.923	0.233	0.930	0.931
2	1.975	0.805	0.226	0.923	0.927
3	2.843	0.691	0.241	0.935	0.935
4	2.730	0.872	0.237	0.958	0.957
5	1.790	0.518	0.318	0.912	0.915
6	2.294	0.828	0.265	0.938	0.932
7	2.287	0.350	0.364	0.928	0.929
8	3.190	0.797	0.257	0.935	0.934
9	2.927	0.919	0.231	0.953	0.968
10	2.813	1.554	0.153	0.918	0.927
11	2.651	0.521	0.342	0.933	0.932
12	2.246	0.628	0.247	0.930	0.925
13	3.543	0.781	0.277	0.941	0.941
14	1.908	0.937	0.212	0.941	0.940
15	3.781	0.792	0.257	0.942	0.940
16	2.822	1.152	0.167	0.935	0.935
17	3.070	0.924	0.214	0.951	0.944
18	2.996	0.842	0.222	0.947	0.924
Average	2.662	0.824	0.248	0.936	0.935

fitting for estimating the tissue kinetic rates and vascular fraction for each cluster TTAC i of the brain volume clustered to a total of 50 clusters. Results are compared with those obtained using plasma-sampled data in place of u_e in the nonlinear fitting.

Linear regression analysis for the estimates of K performed for all 18 subjects and 50 clusters is illustrated in Fig. 3. The measurements of K are highly comparable for all choices of p, with correlation coefficients of 0.97968, 0.99269 and 0.99115, slopes near 1 (0.9735, 0.9832 and 0.9873) and intercepts around 0 (0.0012, 0.00096 and .00074) in each case for $p=1$, 2 and 3. Fig. 3 illustrates the inferiority for $p=1$ and that $p=2$ and $p=3$ are comparable. Thus, we suggest using $p=2$ to minimize cost, without affecting the quality. All other reported results used $p=2$.

4.3. Visual inspection of the input function

A comparison of the estimated input function u_e with the plasma-sampled input u_p is illustrated in Fig. 4. Because these two curves come from different sources, namely CA-ROI and arm arterial plasma samples, there is a time shift between them. In order to provide a better comparison, we automatically shifted u_e to match u_p (Fig. 4B). As expected, the tails of both curves are closer because the tail of the estimated curve is obtained by the fit with the plasma samples. For all subjects, u_e is smoother for a later time

because it is evaluated using a functional form. Additional representative comparisons of u_p with shifted u_e are shown in Fig. 5.

4.4. The model parameters defining u_e

Table 1 presents the estimates for θ, λ and δ. The consistency of δ around the average of 0.248 suggests the robustness of model u_{W_2} with respect to different subjects. We observed that $\alpha^{(i)}$ values are remarkably consistent across all subjects as well as clusters and well within the range prescribed by the constraints. On the other hand, the variation in θ is indicative of the variable partial volume effects because the identified CA-ROIs vary in their location, size and shape between subjects.

4.5. Quantitative evaluation for real data by Patlak analysis

To provide a comparison with the method presented in Reference [9], we used the recovered input for each subject in Patlak analysis for each cluster TTAC. The data of the last three frames (i.e., 15–60 min) were used for the Patlak analysis. The equilibrium of the FDG tracer in this time interval is justified in Reference [20]. Results are compared with those obtained using the plasma-sampled data (see Table 2 for the representative results for the first five subjects). The calculated K values over all clusters and all subjects were highly correlated, with a correlation coefficient of 0.99686, a slope of 0.9878 and an intercept of 0.00071 (Fig. 6). The within-subject variation of K is comparable whether calculated using u_p or u_e. The results are comparable with those presented in Reference [9], in which analysis of CMRglc for one subject yielded an R^2 of 0.9997, a slope of 1.0018 and an intercept of −0.031.

4.6. Quantitative evaluation for real data by nonlinear least squares

To further evaluate the method described in Section 3 for recovering the input function, we used it in the postestimation of K_1, k_2 as well as k_3 and in turn K values, and these values were compared with those in which the plasma-sampled data were used. Table 3 provides the results of linear regression analysis, the slopes, intercepts and correlation coefficients for the calculation of K for the first five subjects over all 50 clusters. Again, the within-subject variation of K is comparable whether calculated by u_p or u_e. Fig. 7 illustrates the regression analysis for individual kinetic rate parameters K_1, k_2 and k_3 for Subject 5.

Table 2
Linear regression analysis comparing calculations of K using the Patlak analysis with input functions u_p and u_e for cluster TTACs

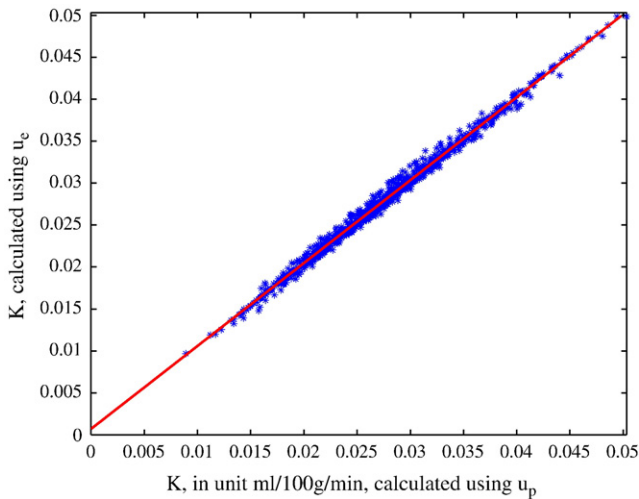| Subject	u_p (K, mean±S.D.)	u_e (K, mean±S.D.)	Correlation coefficient	Slope	Intercept
1	0.033963±0.007409	0.034371±0.007466	0.99996	1.008	0.00015
2	0.024923±0.004949	0.026501±0.005065	0.99887	1.022	0.00130
3	0.023531±0.005635	0.024157±0.005797	0.99997	1.029	−0.00005
4	0.026678±0.003745	0.026811±0.003745	0.99991	1.000	0.00013
5	0.030645±0.005961	0.030775±0.005870	0.99945	0.984	0.00061

Fig. 6. Linear regression for K calculated with u_p as compared with u_e using Patlak analysis. Regression analysis for all subjects and all clusters yielded a high correlation (0.99686, with a slope of 0.9878 and an intercept of 0.00071).

Although not presented here, a careful examination of results obtained with u_e (u_p) showed that in only 2 (0), 8 (8) and 34 (24) of 900 cases were the bounds K_1, k_2 and k_3 attained, which justifies the choice of bounds for the rate constants in the optimization problem.

4.7. Quantitative validation of u_e for simulated data

Kinetic rate parameters, K_1, k_2, k_3, for the first three sets of both gray and white materials from Table 1 in Reference [17] were used for simulation. For each set of rate parameters, we obtained a TTAC using convolution Eq. (3), with u_p substituted for $u(t)$. This yielded six TTACs with known rate parameters and K for each subject. We then used the subject-dependent recovered u_e to estimate K by graphical Patlak analysis and directly from Eq. (2) using the recovered kinetic parameters obtained by weighted nonlinear least squares. This process studied the use of u_e in the postestimation stage for the 50 clusters for each subject, as described in Section 4.6, but with data for which the exact K was known. The calculated K values for all simulation data were well correlated with the true values, with correlation coefficients of 0.96213 and 0.99780, slopes of 0.9943 and 1.019 and intercepts of 0.0015 and −0.000047 for the calculation of K by Patlak analysis and directly using Eq. (2), respectively. The mean and standard deviation values of the relative estimation errors of K are

5.481% (1.676%) and 7.766% (0.301%). The individual rate parameters were quite well correlated, with correlation coefficient and slope pairs for K_1, k_2 and k_3 of 0.94319 and 1.076, 0.89782 and 1.083 and 0.95925 and 1.006, respectively.

5. Discussion

Here we focus on certain specifics of the method described in Section 3.

5.1. Recovering the input function

In the model of the input for u_e, the values v_{τ_p} and v_τ are known and only the parameters θ, λ and δ need to be determined. Rather than using the TTACs to obtain the parameters of this input function, these could be obtained by directly fitting the model u_{W_2} with three plasma samples. In that case, the analytical form for u_{W_2} could be extrapolated to provide values for $t \geq \tau$, with scaling by θ of the linear parts in Eq. (1) for $0 < t \leq \tau$. In Fig. 8, we illustrate for one subject the recovered input function that was obtained by the algorithm described in Section 3 as compared with that obtained directly by data fitting with just the plasma samples and extrapolation. This shows that without information from the TTACs, the data on the early time window are shifted too high ($\theta = 3.909$).

5.2. Time shift between plasma samples and the image-derived TAC

As shown in Figs. 1 and 4, there is always a time shift between the CA-ROI TAC and the measured plasma samples for early time. Should the data on W_1 measured from the CA-ROI be shifted to match those on W_2, which is obtained directly from the three plasma samples? We used the arterial plasma samples to determine that the actual shift for Subject 4 is 10 s. The plasma samples at approximate times 10, 30 and 60 min were 0.7150, 0.4487 and 0.3130 counts/ml/min, respectively. Supposing that all plasma samples for $t > \tau$ were shifted by 10 s to the right and then used in the fit for u_{W_2}, the differences at these same three time points are only −0.004, −0.001 and −0.0005, respectively, with relative errors less than 0.56%. It has been reported that the impact of errors of this magnitude in the input function is insignificant in terms of parametric estimation [21]. We conclude that the time delay between the image-derived curve and plasma samples is negligible.

Table 3
Linear regression analysis comparing calculations of K using Eq. (2) with input functions u_p and u_e for cluster TTACs

Subject	u_p (K, mean±S.D.)	u_e (K, mean±S.D.)	Correlation coefficient	Slope	Intercept
1	0.031580±0.010040	0.032050±0.009939	0.99708	0.987	0.00089
2	0.025624±0.006794	0.027106±0.006846	0.99661	1.004	0.00140
3	0.023363±0.007258	0.023972±0.007333	0.99226	1.002	0.00055
4	0.025738±0.005860	0.025944±0.005823	0.99940	0.993	0.00038
5	0.029736±0.007804	0.029685±0.007336	0.98896	0.930	0.00230

Regression for K_1

Regression for k_2

Regression for k_3
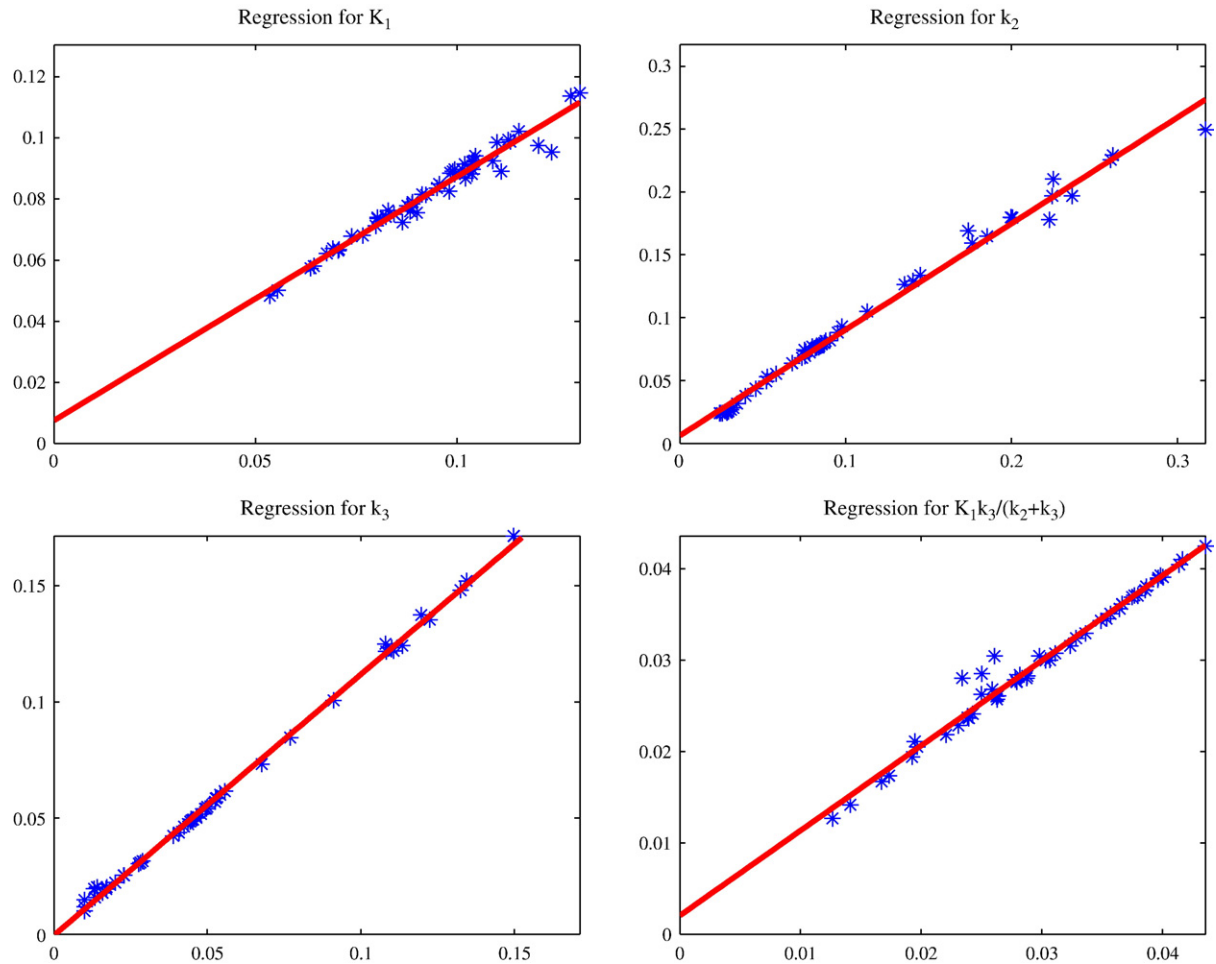
Regression for $K_1 k_3/(k_2+k_3)$

Fig. 7. Comparison of the two sets of parameters calculated by u_e, x-axis, and u_p, y-axis, for Subject 5. The correlation coefficients of these four parameters are 0.98140, 0.99538, 0.99916 and 0.98896.

5.3. Plasma sampling

In this study, we took advantage of the availability of arterial plasma samples to assess all aspects of the method, using the validated compatibility between arterial and venous plasma samples, with a mean difference over all time points of less than 2.25% [9]. Practically, for new studies in which arterial sampling is not already intended, the use of venous, rather than arterial, samples, as described also in Reference [9], is recommended as a less invasive and less painful method of acquiring the necessary data.

5.4. Advantage of using two windows in defining the input function

In the proposed method, we introduced the use of two windows for defining u_e because of the difficulty that arises in finding a single analytical formulation that can give a good model for the tracer concentration in plasma for the entire time duration. The use of the two windows provides more flexibility and less complexity for modeling u_e after the initial half minute, and the first half minute is easily approximated. This approximation on W_1 is a crude
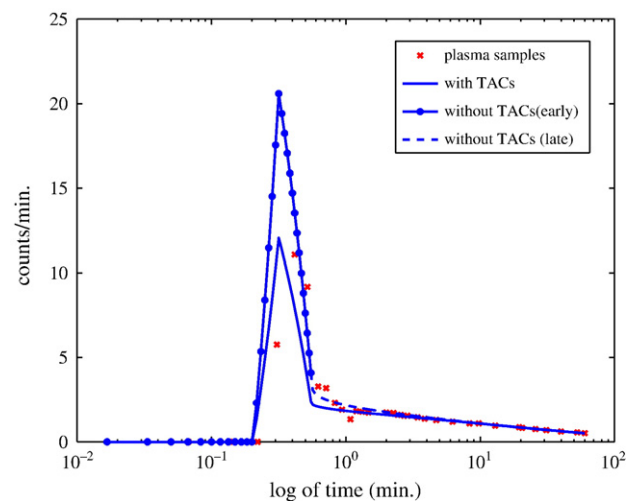
Fig. 8. Comparison of the recovered input function by direct data fitting of the plasma samples ($\theta = 3.909$) and by using the TTACs in the data fitting [Eq. (7)] ($\theta = 2.287$) for Subject 7. The use of the TTACs in the nested optimization yielded a θ that led to a much better fit of the recovered input function with the plasma samples.

simplification, but it is a very good approximation of the real process when τ is very small. Clearly, it is also possible to use higher-order fitting [4] rather than linear approximation on W_1, but with $\tau < 0.6$ min, the impact will be insignificant. On the other hand, for a later time, the image-derived CA-ROI TAC may be contaminated by spillover, and so three samples were used to replace the CA-ROI data. As compared with other image-based input function estimation methods [9–12,22,23] that use the entire CA-ROI TAC for recovery of the input data, the proposed method is free from spillover contamination at a later time.

6. Conclusions

A reliable semiautomated alternative for input function estimation that uses image-derived data augmented with three plasma samples has been presented and validated for FDG-PET human brain studies. A simulated data study validates the recovered input for finding known kinetic values. In contrast to the original method proposed in Reference [9], there is no need to additionally manually determine the tissue ROI near the CA-ROI. The Matlab-based implementation of the tool is available at http://math.asu.edu/~rosie.

References

[1] PET Working Group. PET Working Group: NIH/NIA neuroimaging initiative. URL http://www.nia.nih.gov/ResearchInformation/ExtramuralPrograms/NeuroscienceOfAging/Summary+%E2%80%93+PET+Working+Group.htm, 2005.

[2] Phelps ME, Huang S-C, Hoffman EJ, Selin CE, Kuhl D. Tomographic measurement of local cerebral glucose metabolic rate in man with (^{18}F) fluorodeoxyglucose: validation of method. Ann Neurol 1979; 6:371–88.

[3] Bentourkia M. Kinetic modeling of PET-FDG in the brain without blood sampling. Comp Med Imaging Graph 2006;30:447–51.

[4] Eberl S, Anayat AR, Fulton RR, Hooper PK, Fulham MJ. Evaluation of two population-based input functions for quantitative neurological FDG PET studies. Eur J Nucl Med 1997;24:299–304.

[5] Tsuchida T, Sadato N, Yonekura Y, Nakamura S, Takahashi N, Sugimoto K, et al. Noninvasive measurement of cerebral metabolic rate of glucose using standardized input function. J Nucl Med 1999; 40(9):1441–5.

[6] Riabkov DY, Bella EVRD. Estimation of kinetic parameters without input functions: analysis of three methods for multichannel blind identification. IEEE Trans Biomed Eng 2002;49(11):1318–27.

[7] Feng DG, Wong K-P, Wu C-M, Siu W-C. A technique for extracting physiological parameters and the required input function simultaneously from PET image measurements: theory and simulation study. IEEE Trans Inf Technol Biomed 1997;1(4):243–54.

[8] Wong K-P, Feng D, Meikle SR, Fulham MJ. Simultaneous estimation of physiological parameters and the input function — in vivo PET data. IEEE Trans Inf Technol Biomed 2001;5(1):67–76.

[9] Chen K, Bandy D, Reiman E, Huang SC, Lawson M, Feng D, et al. Noninvasive quantification of the cerebral metabolic rate for glucose using positron emission tomography, ^{18}F-fluorodeoxyglucose, the Patlak method, and an image-derived input function. J Cereb Blood Flow Metab 1998;18:716–23.

[10] Litton J-E. Input function in PET brain-studies using MRI defined arteries. J Comput Assit Tomogr 1997;21(6):907–9.

[11] Wahl LM, Asselin MC, Nahmias C. Regions of interest in the venous sinuses as input functions for quantitative PET. J Nucl Med 1999; 40(10):1666–75.

[12] Asselin MC, Cunningham VJ, Amano S, Gunn R, Nahmias C. Parametrically defined cerebral blood vessels as non-invasive blood input functions for brain PET studies. Phys Med Biol 2004;49(6): 1033–54.

[13] Guo H, Renaut RA, Chen K, Reiman E. Clustering huge data sets for parametric PET imaging. Biosystems 2003;71(1–2):81–92.

[14] Raichle ME, Martin WR, Herscovitch P, Mintun MA, Markham J. Brain blood flow measured with intravenous H$_2^{15}$O: II. Implementation and validation. J Nucl Med 1983;24:790–8.

[15] Guo H, Renaut R, Chen K. Evaluating an alternative model for the input function in FDG-PET studies. 2007. URL http://math.la.asu.edu/~rosie/mypapers/nmbsupp.pdf.

[16] Sokoloff L, Reivich M, Kennedy C, Rosiers MHD, Patlack CS, Pettigrew KD, et al. The [^{14}C]-deoxyglucose method for the measurement of local cerebral glucose metabolism: theory procedures and normal values in the conscious and anesthetized albino rat. J Neurochem 1977;28:897–916.

[17] Huang S-C, Phelps ME, Hoffman EJ, Sideris K, Selin CJ, Kuhl DE. Noninvasive determination of local cerebral metabolic rate of glucose in man. Am J Physiol 1980;238(E):69–82.

[18] Zhou Y, Endres CJ, Brasic JR, Huang S-C, Wong DF. Linear regression with spatial constraint to generate parametric images of ligand-receptor dynamic PET studies with a simplified reference tissue model. NeuroImage 2003;18(4):975–89.

[19] The Mathworks. Optimization Toolbox user's guide, 2005.

[20] Wienhard K, Pawlik G, Herholz K, Wagner R, Heiss, W-D. Estimation of local cerebral utilization by positron emission tomography of ^{18}F-2-fluoro-2-deoxy-D-glucose: a critical appraisal of optimization procedures, J Cereb Blood Flow Metab.

[21] Chen K, Huang S-C, Yu D-C. The effects of measurement errors in the plasma radioactivity curve on parameter estimation in positron emission tomography. Phys Med Biol 1991;36(9):1183–200.

[22] Liptrot M, Adams KH, Martiny L, Pinborg LH, Lonsdale MN, Olsen NV, et al. Cluster analysis in kinetic modelling of the brain: a noninvasive alternative to arterial sampling. Neuroimage 2004;21(2):483–93.

[23] Sanabria-Bohorquez SM, Maes A, Dupont P, Bormans G, de Groot T, Coimbra A, et al. Image-derived input function for [^{11}C]flumazenil kinetic analysis in human brain. Mol Imaging Biol 2003;5(2):72–8.